Simulation of Laser-Induced Thermo-Mechanical Stress During Ultrafast Laser Ablation of Indium Tin Oxide with Transient Optical Properties

Dorian Kürschner*[1], Goran Hallum[2], Heinz Huber[2], and Wolfgang Schulz[1]

[1]*Department NLD, RWTH Aachen University, Steinbachstr. 15, 52074 Aachen, Germany*
[2]*Department of Applied Sciences and Mechatronics, Hochschule München University of Applied Sciences, Lothstr. 34, 80335 Munich, Germany*
**Corresponding author's e-mail: dorian.kuerschner@nld.rwth-aachen.de*

There is still a lack of understanding of a possible mechanical ablation mechanism and the causes of thermal degradation of thin indium tin oxide (ITO) films. A dual hyperbolic two temperature model is applied to the ultrashort pulsed laser ablation process of 100 nm indium tin oxide films. The model describes transient optical properties by taking into account the changes in the complex dielectric function due to laser excitation. The laser excitation is modelled by free electron dynamics and a nonlinear absorption coefficient for a laser pulse duration of 700 fs and a central wavelength of 1056 nm. For peak fluences $F \leq 0.35\,\mathrm{J/cm^2}$, we find that the modeled strain exceeds the yield strain in the regions where the experimental craters show signs of mechanical ablation behavior. For larger peak fluences $F > 0.35\,\mathrm{J/cm^2}$ the model predicts lattice temperatures T_l exceeding the melting temperature $T_{\mathrm{melt,ITO}}$ of indium tin oxide. The computed depth where $T_l \geq T_{\mathrm{melt,ITO}}$ agrees with the measured ablation crater depths.
DOI: 10.2961/jlmn.2023.03.2011
Keywords: ultrashort pulsed laser ablation, two temperature model, elastodynamics, indium tin oxide, electron dynamics, spallation, simulation

1. Introduction

Within the last decades, the growing demand of optoelectronic devices, e.g., for high resolution flat screens on portable computers or thin film photovoltaic applications, promoted the development of various transparent conducting oxides (TCOs). Indium tin oxide (ITO) belongs to the group of TCOs. Due to its high electrical conductivity combined with high optical transparency, it is widely used in optoelectronics, such as thin-film solar cells, display technologies and touch screen devices [1, 2]. However, laser-based fabrication of indium tin oxide devices remains challenging since its optical and electrical properties are highly sensitive to thermal processing. While photolithography is still used for material processing of ITO, it has been mostly replaced by laser structuring [3]. ITO is a semiconductor with a band gap ranging between 3.5 eV to 4.2 eV [4, 5]. The equilibrium free charge carrier density depends on the tin doping content, where the density ranges from $1 \times 10^{20}/\mathrm{cm^3}$ to $1 \times 10^{21}/\mathrm{cm^3}$ [5].

The optical properties of semiconductors are strongly related to their electrical properties depending on the transient free charge carrier density. The free charge carrier density changes as laser radiation is absorbed within the material, leading to excitation of bound electrons into the conduction band. Within the conduction band, the excited electrons can move almost freely through the crystalline lattice. Therefore, these electrons are often called quasi-free electrons, whereas within this manuscript we use the term free electrons. When irradiated by light, the free electrons gain energy via inverse bremsstrahlung absorption. The excited electrons either transfer energy to lattice atoms for further ionization by collisions or recombine. In semiconductors the relevant ionization processes include: single- and multiphoton ionization, collision ionization, radiative recombination, and Auger recombination [6].

1.1. Transient optical properties of ITO films

At a material interface the abrupt change of the dielectric function causes travelling light to be refracted and reflected. The reflectivity of materials depends on polarization. In this manuscript only p-polarized laser radiation is utilized. Therefore, using Fresnel's formulae the reflectivity R of p-polarized light at a single material interface between nonmagnetic medium 1 and medium 2 is described as:

$$R(\varepsilon_1, \varepsilon_2, \alpha_{inc}) = \left| \frac{A_p}{B_p} \right|^2 \tag{1}$$

with ε_i being the (complex) dielectric functions of media 1 and 2, and α_{inc} the angle of incidence, respectively. The factors A_p and B_p are given by:

$$A_p = \sqrt{\varepsilon_1}\cos(\alpha_{inc}) - \sqrt{\varepsilon_1}\sqrt{\varepsilon_2 - \varepsilon_1 \sin^2(\alpha_{inc})} \tag{2}$$

$$B_p = \sqrt{\varepsilon_2}\cos(\alpha_{inc}) + \sqrt{\varepsilon_1}\sqrt{\varepsilon_2 - \varepsilon_1 \sin^2(\alpha_{inc})} \tag{3}$$

In ITO the optical properties at wavelengths in the visible and near infrared are determined by the interaction between photons and the bound as well as the free electrons. Hence, the dielectric function is given by [7]:

$$\varepsilon(\omega, n_e) = \underbrace{\varepsilon_\infty}_{\text{Background}} + \underbrace{\varepsilon_{\mathrm{TL}}(\omega)}_{\text{Bound electrons}} + \underbrace{\varepsilon_{\mathrm{Drude}}(\omega, n_e)}_{\text{Free electrons}} \tag{4}$$

The dielectric function consists of a constant dielectric background ε_∞ and the contribution $\varepsilon_{\mathrm{TL}} = \varepsilon_{\mathrm{TL},1} + i\varepsilon_{\mathrm{TL},2}$ of the

bound electrons modeled by a Tauc-Lorentz oscillator model. Additionally, there is a contribution of free electrons $\varepsilon_{\text{Drude}}$ following the Drude theory. The imaginary part of the contribution from bound electrons $\Im(\varepsilon_{\text{TL}}) = \varepsilon_{\text{TL},2}$ is given by [8]:

$$\varepsilon_{\text{TL},2} = \begin{cases} \frac{AE_0(E-\Delta)^2}{(E^2-E_0^2)^2+C^2E^2} \cdot \frac{1}{E} & E > \Delta \\ 0 & E \leq \Delta \end{cases} \tag{5}$$

where $E = \hbar\omega$ is the photon energy, A, E_0, C correspond to the strength, the resonance frequency and the line broadening of the Lorentzian oscillator, respectively. The real part of the bound electron contribution $\Re(\varepsilon_{\text{TL}}) = \varepsilon_{\text{TL},1}$ can be evaluated using Kramer-Kronig relations. The full analytic solution is given in [8]. The free carrier contribution to the dielectric function of semiconductors is given by the Drude model [9]:

$$\varepsilon_{\text{Drude}}(\omega, n_e) = -\frac{\omega_p^2}{\omega^2 + i\gamma\omega} \tag{6}$$

$$\omega_p(n_e) = \sqrt{\frac{n_e e^2}{\varepsilon_0 m_e^*}} \tag{7}$$

here n_e is the free electron density, ω_p the plasma frequency, γ the damping rate, and m_e^* the effective mass of the free electrons. Here we use $m_e^* = 0.53m_e$ [7]. When the angular frequency ω of the laser radiation reaches the plasma frequency ω_p the transmission at the material surface increases drastically. Hence, the reflectivity of the surface is strongly reduced. The material surface is transparent for angular frequencies greater than the plasma frequency $\omega \geq \omega_p$ explaining the UV-transparency of metal surfaces [9]. The plasma frequency ω_p corresponds to the critical electron density $n_{e,crit}$ where the material surface becomes transparent (c.f. eqs. (6) and (7)). In contrast to the critical electron density of a free electron gas, in doped semiconductors there is a contribution to the dielectric background by bound electrons to the dielectric function and thus the plasma frequency [10]. Hence, the critical electron density of ITO becomes: $n_{e,crit} = \omega^2\varepsilon_{\text{opt}}\varepsilon_0 m_e^*/e^2$ with $\varepsilon_{\text{opt}} = \varepsilon_\infty + \varepsilon_{\text{TL}}(\omega)$ [9, 10]. For the laser wavelength of $\lambda = 1056\,\text{nm}$ the critical electron density equals: $n_{e,crit} \approx 1.90 \times 10^{27}/\text{m}^3$.

Most of the transmitted radiation at the material surface becomes absorbed within the optical penetration depth. The optical penetration depth δ_{opt} is inversely proportional to the imaginary part $\Im$ of the complex refractive index, which itself is the square root of the dielectric function $\Im(\sqrt{\varepsilon})$. The absorption coefficient α_{abs} is given by:

$$\delta_{\text{opt}}(\omega, n_e) = \frac{1}{\alpha_{abs}(\omega, n_e)} \tag{8}$$

$$\alpha_{abs}(\omega, n_e) = \frac{2\omega}{c_0}\Im(\sqrt{\varepsilon(\omega, n_e)}) \tag{9}$$

where c_0 is the speed of light and ω is the angular frequency of the light once again.

1.2. Free electron dynamics

To determine the transient optical properties of the material during the interaction with the laser radiation the transient dielectric function ε has to be known. As the dielectric function ε depends on the free electron density, the temporal evolution of the free electron density $n_e = n_e(t)$ is calculated as a function of the laser intensity I. The corresponding rate equation is given by [6, 11, 12]:

$$\partial_t n_e = w_{\text{SFI}} + w_{\text{imp}} - w_{\text{diff}} - w_{\text{rec}} \tag{10}$$

The first two terms in eq. (10) correspond to the electron generation by absorption of the incoming photons. w_{SFI} is the ionization rate for strong field ionization i.e. multiphoton ionization or tunnel ionization. w_{imp} corresponds to the impact ionization rate. Once there are free electrons in the conduction band, they absorb photons by inverse bremsstrahlung absorption and gain kinetic energy. If the kinetic energy exceeds a critical value of $E_{crit} \approx 1.5\Delta$, collisions with bound electrons lead to ionization [12]. Typically, undoped semiconductors initially only have a small free electron density. Therefore, seed-electrons for the impact ionization are generated by strong field ionization. However, if the free electron density exceeds $1 \times 10^{10}/\text{cm}^3$, impact ionization is the dominant ionization mechanism. Due to doping, the equilibrium free electron density in ITO is in the range of $1 \times 10^{20}/\text{cm}^3$ and strong field ionization can be neglected [7, 13]. The last two terms in eq. (10) are w_{diff}, the "loss" of electrons by diffusion and w_{rec} describes recombination, respectively. For ITO the rate equation reads [7, 11, 12]:

$$\partial_t n_e = r_{\text{imp}} \cdot I \cdot n_e - g_{\text{diff}} \cdot n_e - \eta_{\text{Auger}} \cdot n_e^3 \tag{11}$$

As the acceleration of electrons is not instantaneous but takes time, the electrons which can contribute to ionization are retarded by the time $t_{\text{ret}} = \tau_e \cdot K$. Here K is the number of photons necessary to overcome the band gap Δ (here $\lambda = 1056\,\text{nm} \longrightarrow K = 4$) and τ_e the electron collision time. In a first order approximation r_{imp} is given by [12]:

$$r_{\text{imp}} = \begin{cases} \frac{\alpha_{\text{imp}}}{1+\alpha_{\text{imp}} \cdot t_{\text{ret}}} & V \cdot n_e \geq 0.5 \\ 0 & V \cdot n_e < 0.5 \end{cases} \tag{12}$$

$$\alpha_{\text{imp}} = \frac{1}{\omega^2\tau_e^2 + 1}\frac{e^2\tau_e}{c_0 n_0 m_e^* \Delta} \tag{13}$$

The impact ionization is considered only if the probability of finding an electron in the focal volume $V = \pi w_0^2 \delta_{\text{thick}}$ is greater than 50%. The focal volume V depends on the beam radius of the laser beam w_0 and the thickness δ_{thick} of the ITO-film. Further, $\tau_e = 1/\gamma$ is the electron collision time, e the electron charge, ω the angular frequency of the incident photons, c_0 the speed of light in vacuum, n_0 the refractive index, m_e^* the effective electron mass and Δ the band gap, respectively. In fact, τ_e, n_0 and Δ depend on the free electron density [7, 14, 15]:

$$\gamma(n_e) = \frac{1}{\tau_e(n_e)} = \gamma_{\text{max}} \cdot \frac{n_e}{n_e + \beta n_{e,crit}} \tag{14}$$

$$n_0(n_e) = \sqrt{\varepsilon(n_e)} \tag{15}$$

$$\Delta(n_e) = \Delta_0 + \Delta_{\text{BM}}(n_e) \tag{16}$$

$$\Delta_{\text{BM}}(n_e) = \frac{\hbar^2}{2m_e^*}\left(3\pi^2 n_e\right)^{\frac{2}{3}} \tag{17}$$

The electron collision time τ_e (inverse of the electron collision frequency γ) reduces with increasing free electron

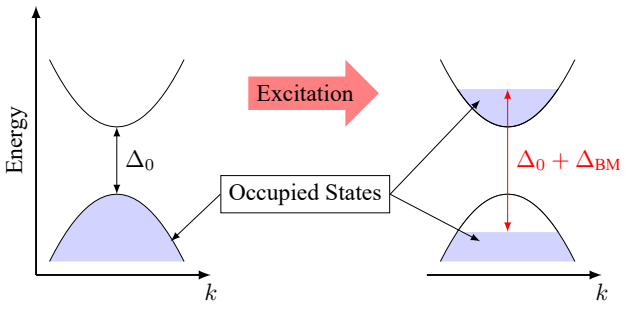

Fig. 1 Schematic illustration of the Burstein-Moss effect. As a result of excitation of electronic states to the conduction band and Pauli's exclusion principle the effective band gap Δ increases with respect to the intrinsic material band gap Δ_0. After [16].

density because it is more likely to collide with other particles. As described in [15] γ saturates at a material dependent maximum value γ_{max}. The excited electron densities during and after the laser pulse exceed the critical electron density $n_{e,crit}$. Therefore, the electron collision time τ_e depends weakly on the electron density and is assumed to be equal to $\tau_e \approx 1/\gamma_{\text{max}} = 3.36\,\text{fs}$ (c.f. eq. (14)).

As a result of ionization, the lower energy states in the conduction band are already occupied. Due to Pauli's exclusion principle, further ionization can only happen if the electrons are excited to higher energy states. Therefore, the band gap increases if the number of free electrons in the conduction band increases. This effect is called Burstein-Moss effect and is schematically depicted in fig. 1. The increase of the bandgap Δ causes a reduction of the impact ionization rate and a change of optical properties (c.f. eqs. (5) and (13)).

Finally, the diffusion rate coefficient g_{diff} in eq. (11) is given by [11]:

$$g_{\text{diff}} = \frac{\tau_e \Delta}{3 m_e^*} \left(\left(\frac{2.4}{w_0} \right)^2 + \left(\frac{1}{\delta_{\text{thick}}} \right)^2 \right) + \frac{1}{\omega^2 \tau_e^2 + 1} \cdot \frac{m_e^* \omega^2 \tau_e}{M_{\text{mol}}} \tag{18}$$

with $M_{\text{mol}} = 7.14 \times 10^{-25}\,\text{kg}$ being the molecular mass for ITO [17], w_0 the laser beam radius and δ_{thick} the film thickness, respectively.

1.3. Ultrafast thermoelasticity model

Since its formulation in the middle fifties, the two temperature model (TTM) has found extensive use in modelling the heat induced into materials during laser-matter interaction. As the timescale for laser pulses became shorter into the subnanosecond range, the temporal relaxation of the heat flow in Fourier's law has to be taken into account [18, 19, 20]:

$$\tau \partial_t \boldsymbol{q} + \boldsymbol{q} = -k \boldsymbol{\nabla} T \tag{19}$$

The lateral dimensions of the thin film are much larger than its film thickness δ_{thick}. The time for the lateral waves to travel to the material boundary and reflect back is much larger than the time for the one dimensional motion in the thickness direction. Thus, the assumption of a one dimensional problem is appropriate [19, 21]. In one dimension there is only one direction in which movement is possible. Therefore, only longitudinal waves are considered. The equations for the electronic and lattice temperatures (T_e, T_l) and heat fluxes (q_e, q_l) read [20]:

$$C_e \partial_t T_e = -\partial_z q_e - G(T_e - T_l) + Q_{\text{Heat}}(z,t) - Q_{\text{e,ion}} \tag{20}$$

$$\tau_e \partial_t q_e = -k_e \partial_z T_e - q_e \tag{21}$$

$$C_l \partial_t T_l = -\partial_z q_l + G(T_e - T_l) \tag{22}$$

$$\tau_l \partial_t q_l = -k_l \partial_z T_l - q_l \tag{23}$$

Here C_e, C_l are the specific heat capacities, k_e, k_l the thermal conductivities, τ_e and τ_l the collision times for the electronic and lattice subsystems, respectively. Furthermore, G is the coupling between the two subsystems. Excitation of bound electrons into the conduction band requires the energy density $Q_{\text{e,ion}} = \partial_t(\Delta(n_e) \cdot n_e)$ [6]. Furthermore, $Q_{\text{Heat}}(z,t)$ corresponds to the volumetric heat source:

$$Q_{\text{Heat}}(z,t) = \frac{1-R}{\delta_{\text{opt}}} \cdot I(z,t) \tag{24}$$

$$I(z,t) = I_0 \cdot \exp\left(-4 \ln(2) \frac{(t-t_0)^2}{\tau_p^2} \right) \cdot \exp\left(-\frac{z}{\delta_{\text{opt}}} \right) \tag{25}$$

Here I_0 is the peak intensity of the laser pulse, τ_p the pulse duration and $t_0 = 2\tau_p$ the time when the peak intensity is reached. Typically, the temperatures remains constant before melting or evaporation despite further addition of heat into the system due to the latent heat Q_L. The reason is that breakage of inter-atomic bonds via melting or evaporation requires energy. At the phase transition, neglecting changes in pressure and volume, the enthalpy H can be written as: $\mathrm{d}H = C_l(T)\mathrm{d}T$ (here the specific heat capacity is measured in $\text{J}/(\text{m}^3\,\text{K})$). The enthalpy H typically shows a jump at the phase transition while the temperature T remains constant. To numerically resolve the jump we assume a smeared out transition with a temperature width of $\Delta T = T_s - T_{\text{liq}}$. As the literature search was not successful for the solidus and liquidus temperatures T_s and T_{liq} for ITO we assume $\Delta T = 50\,\text{K}$. Thus, the Dirac delta function at the jump becomes a Gaussian distribution leading to a modified the specific heat of the material [22, 23]:

$$C_l(T_l) = C_{l,0} + \frac{\rho Q_L}{\sqrt{\pi}\Delta T} \exp\left(-\left(\frac{T_l - T_{\text{melt}}}{\Delta T} \right)^2 \right) \tag{26}$$

A rise in temperature of a material leads to thermal expansion. In the case of local heating of a material with an ultrashort laser pulse the thermal expansion causes a strong pressure wave to propagate within the material. Additionally, the excitation of electrons from the valence to the conduction band causes the band structure to change. As the electrons gain kinetic energy by inverse bremsstrahlung absorption, they move through the lattice and cause a further lattice deformation. A mathematical description based on the Boltzmann equation is given in [24]. Additionally, plasticity should be

considered as most materials show dynamic hardening behavior and nonlinear stress strain relations for large strains. This could be achieved e.g. via molecular dynamic simulations. However, for these simulations precise knowledge of the interaction and chemical potentials is necessary, which, to the best of our knowledge, is not known for ITO. Therefore, in the scope of this manuscript the nonlinear behavior is omitted. The linearly elastic equation for the lattice motion during and after the laser pulse are thus given by [19]:

$$\rho\partial_t^2 u = (\lambda_1 + 2\mu_2)\partial_z^2 u - (3\lambda_1 + 2\mu_2)\alpha_{\text{th}}\partial_z T_l \tag{27}$$

with ρ being the mass density, u the lattice displacement, λ_1, μ_2 the first and second Lamé constants, and α_{th} the thermal expansion coefficient, respectively.

By using the consistency relation for the strain $\epsilon_{zz} = \partial_z u$ and the velocity $v = \partial_t u$, eq. (27) can be rewritten into a set of first order differential equations:

$$\partial_t u = v \tag{28}$$
$$\rho\partial_t v = (\lambda_1 + 2\mu_2)\partial_z \epsilon_{zz} - (3\lambda_1 + 2\mu_2)\alpha_{\text{th}}\partial_z T_l \tag{29}$$
$$\partial_t \epsilon_{zz} = \partial_z v \tag{30}$$

As already mentioned, this manuscript only considers one dimensional and therefore uni-axial strain into z-direction:

$$\epsilon_{zz}(z,t) \neq 0, \quad \epsilon_{xx} = \epsilon_{yy} = \epsilon_{xy} = \epsilon_{xz} = \epsilon_{yz} = 0 \tag{31}$$

With this the stress-strain relations for an isotropic material becomes [19]:

$$\sigma_{xx} = \sigma_{yy} = \lambda_1 \epsilon_{zz} - (3\lambda_1 + 2\mu_2)\alpha_{\text{th}}(T_l - T_0) \tag{32}$$
$$\sigma_{zz} = (\lambda_1 + 2\mu_2)\epsilon_{zz} - (3\lambda_1 + 2\mu_2)\alpha_{\text{th}}(T_l - T_0) \tag{33}$$

with $T_0 = 300\,\text{K}$ being the environment temperature. As an indicator for material failure the effective stress is defined as:

$$\sigma_{\text{eff}} = |\sigma_{zz} - \sigma_{xx}| = 2\mu_2|\sigma_{zz}| \tag{34}$$

For convenience eqs. (20) to (23) and (28) to (30) are rewritten into conservation form:

$$\partial_t \boldsymbol{Q} + \underline{\boldsymbol{A}}\partial_z \boldsymbol{Q} = \boldsymbol{S} \tag{35}$$
$$\boldsymbol{Q} = (T_e, q_e, T_l, q_l, v, \epsilon_{zz})^T \tag{36}$$
$$\underline{\boldsymbol{A}} = \begin{pmatrix} 0 & \frac{1}{C_e} & 0 & 0 & 0 & 0 \\ \frac{k_e}{\tau_e} & 0 & 0 & 0 & 0 & 0 \\ 0 & 0 & 0 & \frac{1}{C_l} & 0 & 0 \\ 0 & 0 & \frac{k_l}{\tau_l} & 0 & 0 & 0 \\ 0 & 0 & \frac{(3\lambda_1+2\mu_2)\alpha_{\text{th}}}{\rho} & 0 & 0 & \frac{\lambda_1+2\mu_2}{\rho} \\ 0 & 0 & 0 & 0 & 1 & 0 \end{pmatrix} \tag{37}$$
$$\boldsymbol{S} = \begin{pmatrix} \frac{1}{C_e}G(T_e - T_l) + Q_{\text{Heat}} \\ -\frac{1}{\tau_e}q_e \\ \frac{1}{C_l}G(T_e - T_l) \\ -\frac{1}{\tau_l}q_l \\ 0 \\ 0 \end{pmatrix} \tag{38}$$

To solve eq. (35) numerically, we use the following initial conditions:

$$T_e(z, t=0) = T_0 = 300\,\text{K} \tag{39}$$
$$T_l(z, t=0) = T_0 = 300\,\text{K} \tag{40}$$
$$q_e(z, t=0) = 0 \tag{41}$$
$$q_l(z, t=0) = 0 \tag{42}$$
$$v(z, t=0) = 0 \tag{43}$$
$$\epsilon_{zz}(z, t=0) = 0 \tag{44}$$

Furthermore, proper boundary conditions have to be given. During the heating process, heat losses to the surface of the ITO film are neglected [19]:

$$q_e(z=0, t) = 0 \tag{45}$$
$$q_l(z=0, t) = 0 \tag{46}$$

Additionally, the front surface of the film is assumed to be stress-free:

$$\sigma_{zz}(0, t) = 0 \tag{47}$$

For the strain in z-direction ϵ_{zz} this implies (c.f. eq. (33)):

$$\epsilon_{zz}(z=0, t) = \frac{3\lambda_1 + 2\mu_2}{\lambda_1 + 2\mu_2}\alpha_{\text{th}}\left(T_l(z=0, t) - T_0\right) \tag{48}$$

The lower end of the computational domain ($z > \delta_{\text{thick}}$) has absorbing boundary conditions for the mechanical wave and the thermal heat fluxes that are adapted from [25].

The functions used to describe the dynamical electronic properties are:

$$C_e(T_e, n_e) = \frac{\pi^2 k_{\text{B}}}{2T_f} T_e n_e \tag{49}$$
$$T_f(n_e) = \frac{E_f}{k_{\text{B}}} = \frac{\hbar^2 \left(3\pi^2 n_e\right)^{\frac{2}{3}}}{2m_e^* k_{\text{B}}} \tag{50}$$
$$k_e(T_e, n_e) = \frac{\pi^2 k_{\text{B}}^2 \tau_e(n_e) T_e n_e}{3m_e^*} \tag{51}$$

where $k_{\text{B}}, \hbar$ are the Boltzmann and Planck's constants, T_f, E_f the Fermi temperature and energy and m_e^* the effective electron mass.

2. Materials and methods

In this study commercially available ITO samples from *Präzisions Glas & Optik GmbH, Iserlohn, Germany* are investigated. The samples have a sheet resistance smaller than $20\,\Omega/\square$. They consist of a sputtered ITO layer with a thickness of 105 nm on a 25 nm SiO_2 passivation layer on top of a 1.1 mm float glass substrate. The static optical material properties for eqs. (5) and (6) were calibrated from a UV-Vis-measurement by using a Levenberg-Marquard least square optimization in [7]. The relevant material properties for the electronic, thermal and mechanical models are summarized in tables 2 and 3. To the best of our knowledge the lattice collision time τ_l is not known for ITO and SiO_2. Therefore, we use the values for gold [19]. For the substrate we use the material properties of SiO_2. The electron phonon coupling for ITO was estimated for electron temperatures ranging from 300 K

Table 1 Relevant optical material and laser properties of ITO

Symbol	Value	Ref.
ε_∞	1.96	[7]
A	190.02 eV	[7]
E_0	5.07 eV	[7]
C	1.20×10^{-5} eV	[7]
Δ	3.75 eV	[7]
ω_p	2.02×10^{15} rad/sec	[7]
γ	1.70×10^{14} rad/s	[7]
β	0.1	[7]
γ_{max}	2.98×10^{14} rad/s	[7]
δ_{thick}	105 nm	

Table 2 Relevant laser properties of the experimental setup

Symbol	Value
λ	1056 nm
τ_p	700 fs
F	0.32 J/cm^2 to 4.3 J/cm^2
w_0	15 µm

Table 3 Relevant thermal and mechanical properties of ITO and SiO_2

Symbol	Value	Ref.
k	3.95 W/(m K)	[26]
$C_{\text{l,ITO}}$	2.58×10^6 J/(m^3 K)	[26]
τ_l	38.7 ps	[19]
G	3.23×10^{16} W/(m^3 K)	
ρ	7.1 g/cm^3	[27]
E_{y}	175×10^9 Pa	[27]
ν_{poisson}	0.31	[27]
α_{th}	5.81×10^{-6}/K	[28]
$T_{\text{melt,ITO}}$	2100 K	[29]
$Q_{\text{L,ITO}}$	5×10^5 J/kg	[22]
ρ_{SiO2}	2.219 g/cm^3	[27]
$C_{\text{l,SiO2}}$	2.68×10^6 J/(m^3 K)	[30]
$Q_{\text{L,ITO}}$	4.81×10^5 J/kg	[31]
$E_{\text{y,SiO2}}$	78.10×10^9 Pa	[32, 33]
ν_{SiO2}	0.179	[32, 33]
$\alpha_{\text{th,SiO2}}$	5.246×10^{-7}/K	[34]
$T_{\text{melt,SiO2}}$	2273 K	[31]

to 6500 K using eq. (8) in [29]: $G = 3.23 \times 10^{16}$ W/(m^3 K). The temperature dependencies for the lattice thermal conductivities of the ITO film and the SiO_2 substrate are calculated with: $k_l = k - k_e$. The thermal conductivity for SiO_2substrate was taken from [35]. The lattice specific heat capacities for ITO and SiO_2 are $C_{\text{l,ITO}} = 2.575 \times 10^6$ J/(m^3 K) and $C_{\text{l,SiO2}} = 2.68 \times 10^6$ J/(m^3 K) , respectively [26, 30]. The latent heat for the materials is given by $Q_{\text{L,ITO}} = 5 \times 10^6$ J/kg and $Q_{\text{L,SiO2}} = 4.81 \times 10^5$ J/kg [22, 31].

From Young's modulus E_{y} and Poisson's number ν_{poisson} the Lamé coefficients λ_1 and μ_2 are evaluated by using the relations [36]:

$$\lambda_1 = \frac{E_{\text{y}} \nu_{\text{poisson}}}{(1 + \nu_{\text{poisson}})(1 - 2\nu_{\text{poisson}})} \tag{52}$$

$$\mu_2 = \frac{E_{\text{y}}}{2(1 + \nu_{\text{poisson}})} \tag{53}$$

giving $\lambda_1 = 1.09 \times 10^{11}$ Pa and $\mu_2 = 6.68 \times 10^{10}$ Pa for ITO and $\lambda_1 = 1.85 \times 10^{10}$ Pa, $\mu_2 = 3.31 \times 10^{10}$ Pa for SiO_2. The ablation experiments are carried out with a Nd:glass femtosecond laser (*femtoREGEN, Spectra-Physics Inc.*) with a central wavelength of (1056.0 ± 0.5) nm with a spectral full width at half maximum (FWHM) of (5.0 ± 0.5) nm (*BLUE-Wave, StellarNet Inc.*) and a FWHM-pulse duration of (700 ± 100) fs (*pulseCheck, APE GmbH*). A more detailed description on the experimental setup can be found in [37, 38]. The ablation crater profiles are measured with an atomic force microscope (AFM).

To solve the hyperbolic problem (eq. (35)), a global Lax Friedrich finite difference scheme with adaptive time step control was combined with a Predict-Evaluate-Correct-Evaluate (PECE) method. A suitable time step is evaluated from the Courant-Friedrichs-Lewy-Condition (CFL-condition) with $\zeta = 0.5$ and the eigenvalues α_i of the system matrix $\underline{\boldsymbol{A}}$ to ensure numerical stability:

$$\Delta t = \zeta \frac{\Delta z}{\max(\{\alpha_1, \alpha_2, \alpha_3, \alpha_4, \alpha_5, \alpha_6\})} \tag{54}$$

$$\alpha_1 = -\sqrt{k_e/(\tau_e \cdot C_e)} \qquad \alpha_2 = \sqrt{k_e/(\tau_e \cdot C_e)}$$
$$\alpha_3 = -\sqrt{k_l/(\tau_l \cdot C_l)} \qquad \alpha_4 = \sqrt{k_l/(\tau_l \cdot C_l)}$$
$$\alpha_5 = -\sqrt{(\lambda_1 + 2\mu_2)/\rho} \qquad \alpha_6 = \sqrt{(\lambda_1 + 2\mu_2)/\rho}$$

The numerical domain is ranging from $z \in [0, L]$ with $L =$ 200 nm and divided into $n_x = 201$ increments. The change of material properties at the material interface is considered by involving the material properties into the system matrix $\underline{\boldsymbol{A}}$. Each entry $a_{i,j}$ of the system matrix $\underline{\boldsymbol{A}}$ is a diagonal matrix $a_{i,j} = (n_x \times n_x)$with the corresponding material properties for each depth increment.

3. Results

3.1. Measured ablation craters

Figure 2 shows the measured single pulse ablation craters for peak fluences ranging from 0.32 J/cm^2 to 4.3 J/cm^2. The craters were measured by using an AFM. All measured ablation craters show sharp vertical transitions at the positions where the first and second plateaus are reached. Furthermore,

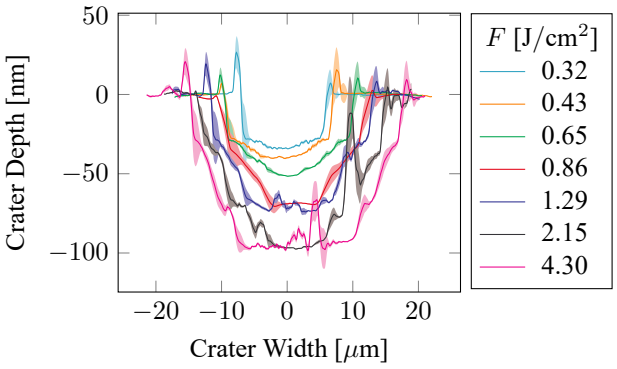

Fig. 2 Measured single pulse ablation craters with an AFM for peak fluences in ranging from $0.32\,\mathrm{J/cm^2}$ to $4.3\,\mathrm{J/cm^2}$. Three depth plateaus are revealed: first plateau at 30 nm, second plateau at 70 nm and a third plateau at 100 nm, which is equal to the ITO layer thickness.

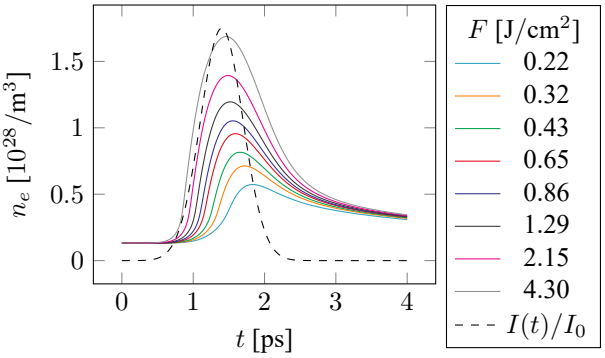

Fig. 3 Temporal evolution of the free electron density n_e at the material surface (z = 0) for different peak fluences, ranging from $0.22\,\mathrm{J/cm^2}$ to $4.3\,\mathrm{J/cm^2}$.

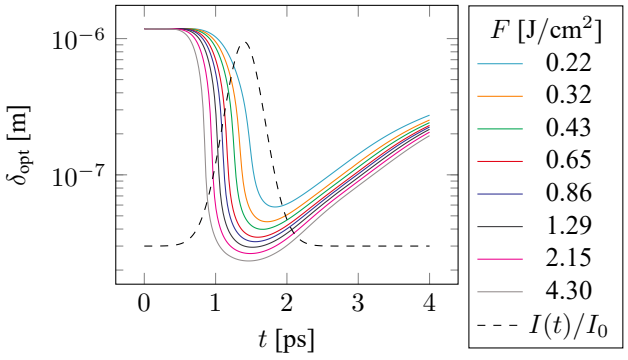

Fig. 4 Computation of the temporal evolution of the optical penetration depth $\delta_{\mathrm{opt}} = \delta_{\mathrm{opt}}(n_e(t))$ for laser pulses with different peak fluences, ranging from $0.22\,\mathrm{J/cm^2}$ to $4.3\,\mathrm{J/cm^2}$.

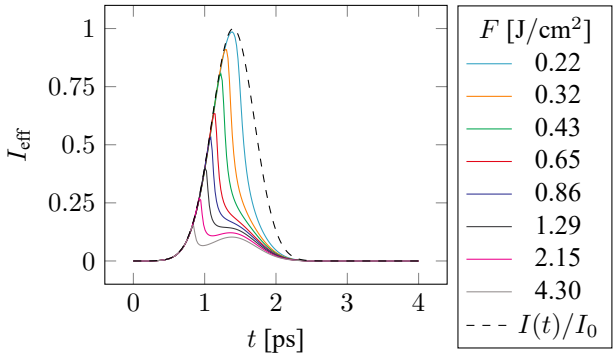

Fig. 5 Computation of the temporal evolution of the scaled transmitted intensity at the sample surface $(z = 0)$ $I_{\mathrm{eff}} = (1 - R(n_e(t))) \cdot I(t)/I_0$ for laser pulses with different peak fluences, ranging from $0.22\,\mathrm{J/cm^2}$ to $4.3\,\mathrm{J/cm^2}$.

all craters show ridge formation with a height of 15 nm to 35 nm in the adjacent region around the crater. For a peak fluence of $F = 0.32\,\mathrm{J/cm^2}$ a flat crater profile is observed with a depth of about 30 nm. This is an indication for a mechanical ablation mechanism, such as spallation [39]. For $F = 1.29\,\mathrm{J/cm^2}$ a second plateau is found at a depth of about 70 nm. For even greater peak fluences ($2.15\,\mathrm{J/cm^2}$, $4.3\,\mathrm{J/cm^2}$), the ITO-layer is fully ablated. The thickness δ_{thick} of the ITO films was measured by calibration of optical measurements to $\delta_{\mathrm{thick}} = 105$ nm in [7]. However, the crater depth around for the peak fluences $F = 2.15\,\mathrm{J/cm^2}$ and $4.3\,\mathrm{J/cm^2}$ equals $z = \delta_{\mathrm{thick}} = 100$ nm. For this reason we use $\delta_{\mathrm{thick}} = 100$ nm for the calculations.

3.2. Free electron dynamics

To compute an accurate heat source (eq. (24)) for the TTM free electron dynamics have to be considered. The temporal evolution of the free electron density n_e is evaluated by solving eq. (11) using eqs. (14) and (25). The results for n_e for peak fluences ranging from $0.22\,\mathrm{J/cm^2}$ to $4.3\,\mathrm{J/cm^2}$ are shown in fig. 3. The used laser parameters are: $\tau_p = 700$ fs, $\lambda = 1056$ nm and $w_0 = 15\,\mu$m. From the results of the free electron density n_e the corresponding optical penetration depth $\delta_{\mathrm{opt}}(n_e)$ and effective intensity I_{eff} penetrating the sample surface $I_{\mathrm{eff}} = (1 - R(n_e(t))) \cdot I(t)/I_0$ are shown in figs. 4 and 5, respectively. According to eqs. (4) and (8) the optical penetration depth decreases as the free electron density increases. Starting at $\delta_{\mathrm{opt}} = 2.2\,\mu$m, the optical penetration depth is reduced to 58 nm (for $F = 0.32\,\mathrm{J/cm^2}$) and 24 nm (for $F = 4.3\,\mathrm{J/cm^2}$). The minimal optical penetration depth as a function of the fluence can be found in fig. 4. Simultaneously, the reflectivity increases drastically after n_e exceeds the critical electron density leading to a strong reduction of the intensity transmitted through the ITO-air-interface leading to a reflectivity of up to 90% for $F = 4.3\,\mathrm{J/cm^2}$.

3.3. Two temperature model

Using the transient optical reflectivity $R(n_e(t))$ and optical penetration depth $\delta_{\mathrm{opt}}(n_e(t))$ from section 3.2, the heat source in eq. (24) becomes to:

$$Q_{\mathrm{Heat}}(z,t) = \frac{1 - R(n_e(t))}{\delta_{\mathrm{opt}}(n_e(t))} \cdot I(z,t) \tag{55}$$

with $I(z,t)$ given in eq. (25). The computed lattice temperatures and resulting strains for the peak fluences $F = 0.22\,\mathrm{J/cm^2}$ and $F = 0.35\,\mathrm{J/cm^2}$ are shown in figs. 7a, 7b, 8a and 8b, respectively. Peak fluences larger than $F \geq 0.43\,\mathrm{J/cm^2}$ result in melting temperatures $T_l \geq T_{\mathrm{melt,ITO}}$.

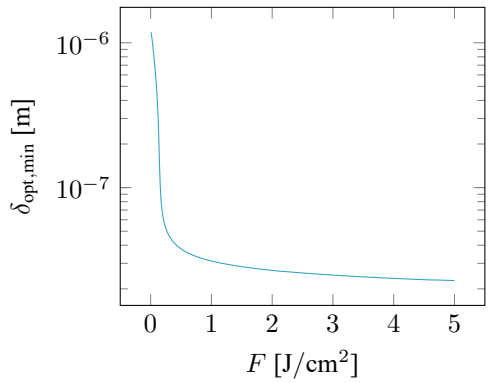

Fig. 6 Minimum optical penetration depth of the ITO film for different peak fluences.

Then, the computed strains and stresses obtained from the full elastic model are questionable, since plastic deformations and melting occur. For this reason, only the computed lattice temperatures are shown for peak fluences $F > 0.35\,\mathrm{J/cm^2}$ and the strains are omitted.

The laser pulse is heating the electronic subsystem and subsequently the heat is transferred to the lattice due to electron-phonon collisions. The lattice reaches its maximum temperature around $t = 12\,\mathrm{ps}$ for a peak fluence of $F = 0.22\,\mathrm{J/cm^2}$ and melting temperature $T_{\text{melt,ITO}}$ at earlier times for larger peak fluences. The times and depths where the melting temperature $T_l \geq T_{\text{melt,ITO}} = 2100\,\mathrm{K}$ of ITO is reached are indicated with the red contour line in figs. 7d to 7f [29]. The melting temperature for SiO_2 equals $T_{\text{melt,SiO2}} = 2273\,\mathrm{K}$ and was not reached for the used fluences [31]. The rise in the lattice temperature leads to thermal expansion of the material. This causes thermoelastic strains and stresses within the ITO film. A study for 105 nm ITO films on flexible polyester substrates identified a yield strain of $\epsilon_{yield} = 2.2\%$ for film breakage [40]. However, we find $\epsilon_{yield} = 2.45\%$ by comparison of the computed values and the measured ablation craters. The region where $\epsilon_{zz} \geq \epsilon_{yield}$ is shown by the red contour lines in the respective ϵ_{zz}-graphs figs. 8a and 8b.

4. Discussion

The increasing free electron density n_e to values exceeding the critical electron density $n_{e,crit}$ simultaneously reduces the optical penetration depth while increasing the reflectivity of the ITO-air-interface. This is a feature of the Drude model in the dielectric function of ITO and indicates metal-like material properties of the ITO film. Before laser excitation, the optical penetration depth is $\delta_{\text{opt}} = 2.2\,\mu\mathrm{m}$ and therefore much larger than the ITO film thickness of $\delta_{\text{thick}} = 105\,\mathrm{nm}$ (c.f. fig. 4). Consequently, heating of the whole film is the result in the TTM. In order to prevent the model from predicting lattice temperatures in the order of several thousand kelvin, the latent heat had to be incorporated into the model.

Feedback of transient mechanical properties onto the index of refraction is not yet covered by the presented model.

In general, mechanical material breakage includes plastic deformations before material failure. However, this not only depends on the strain but also on the strain rate, which is not negligible during ultrashort laser heating [19]. To the best of our knowledge, the dependencies of plastic deformations and material failure on the strain rate have not been reported for ITO yet. For this reason, we use the condition $\epsilon_{zz} \geq \epsilon_{yield}$ as an ablation criteron for Fluences $F \leq 0.35\,\mathrm{J/cm^2}$. Further experimental and numerical studies of the components of the constitutive tensor and plastic behavior of ITO should be carried out in the future.

According to the Gaussian fluence distribution, the fluence decreases in radial direction from the beam center. The fluence at the measured crater radii for the different peak fluences in fig. 2 equals $0.22\,\mathrm{J/cm^2}$. For $F = 0.22\,\mathrm{J/cm^2}$ the thermoelastic model predicts strains exceeding the yield strain $\epsilon_{zz} \geq \epsilon_{yield} = 2.45\%$ in the depths around from $z = 30\,\mathrm{nm}$ while the strains for smaller peak fluences result in $\epsilon_{zz} < \epsilon_{yield}$. This depth agrees with the measured crater ablation depths (c.f.fig. 2) and implies that the ablation mechanism for peak fluences $F < 0.43\,\mathrm{J/cm^2}$ is mechanical in nature. Furthermore, the change of the mechanical material properties causes the pressure wave to be reflected at the material interface. The reflection can be seen in fig. 8a around $t \approx 10\,\mathrm{ps}$. The reflected wave travels towards the sample surface at $z = 0$, where it is fully reflected and leads to a maximum strain value at around $t \approx 20\,\mathrm{ps}$. At this time the pump probe reflectivity of the sample surface is drastically reduced [37]. The mechanical reflectivity R_{mech} is given by [41]:

$$R_{\text{mech}} = \frac{Z_{\text{SiO}_2} - Z_{\text{ITO}}}{Z_{\text{SiO}_2} + Z_{\text{ITO}}} \tag{56}$$

Here Z_{ITO} and Z_{SiO_2} are the impedances $Z = c_{\text{s}}\rho$ of ITO and SiO_2, respectively. c_{s} corresponds to the speed of sound for p-waves and is related to the mass density ρ, Young's modulus E_{y} and Poisson's number ν_{poisson}:

$$c_{\text{s}} = \sqrt{\frac{E_{\text{y}}(1-\nu_{\text{poisson}})}{\rho(1+\nu_{\text{poisson}})(1-2\nu_{\text{poisson}})}} \tag{57}$$

Despite the differences in Young's moduli and Poisson ratios for ITO and SiO_2 (c.f. table 3) the sound velocities of both materials are very similar: $c_{\text{s,ITO}} = 5845.03\,\mathrm{m/s}$ and $c_{\text{s,SiO2}} = 6179.92\,\mathrm{m/s}$. Thus, there is only a weak refraction of the mechanical wave, which is evident in a slightly different slope of the computed strain waves in figs. 8a and 8b. The time the wave needs to travel through the ITO layer is $t = \delta_{\text{thick}}/c_{\text{s,ITO}} \approx 17\,\mathrm{ps}$. This can also be seen in fig. 8a and fig. 8b. Moreover, $c_{\text{s,ITO}}$ and $c_{\text{s,SiO2}}$ result in reflectivity of the mechanical wave: $R_{\text{mech}} \approx 0.5$. Additionally, it should be noted that the used Lax Friedrich scheme exhibits some numerical dissipation, which prevents oscillations but also leads to a small reduction of the computed values over time. Lattice temperatures larger than melting temperature $T_l > T_{\text{melt,ITO}}$ are reached for peak fluences $F \geq 0.43\,\mathrm{J/cm^2}$. In the center of the laser pulse the computed depths z where $T_l(z,t) = T_{\text{melt,ITO}}$ for pulses with $F = 0.43\,\mathrm{J/cm^2}$, $F = 0.65\,\mathrm{J/cm^2}$ and $0.86\,\mathrm{J/cm^2}$ are $z = 39\,\mathrm{nm}$, $z = 63\,\mathrm{nm}$ and $z = 70\,\mathrm{nm}$. The measured ablation crater depths are $z = 37\,\mathrm{nm}$, $z = 49\,\mathrm{nm}$ and $z = 69\,\mathrm{nm}$, respectively (c.f.fig. 2). For this reason, we identify $T_l \geq T_{\text{melt,ITO}}$ as the ablation criterion in this fluence domain. The predicted depths for $F = 1.29\,\mathrm{J/cm^2}$ the

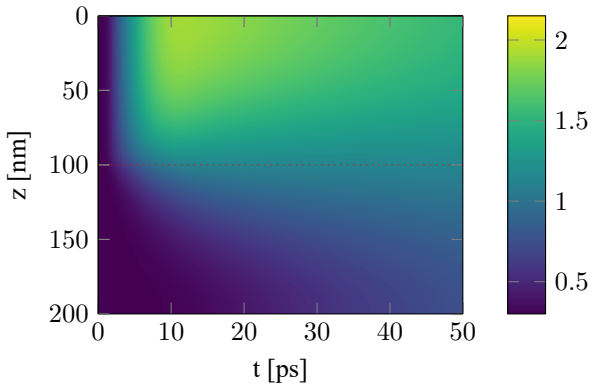

(a) Lattice temperature T_l for a peak fluence of $F = 0.22\,\mathrm{J/cm^2}$. The maximum reached temperature is $T_{l,\max} = 1908.6\,\mathrm{K}$.

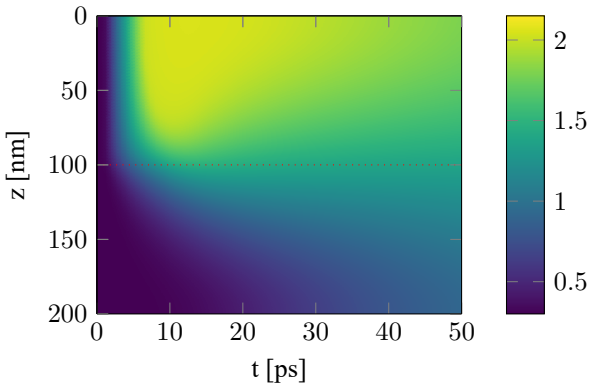

(b) Lattice temperature T_l for a peak fluence of $F = 0.32\,\mathrm{J/cm^2}$. The maximum reached temperature is $T_{l,\max} = 2056.6\,\mathrm{K}$.

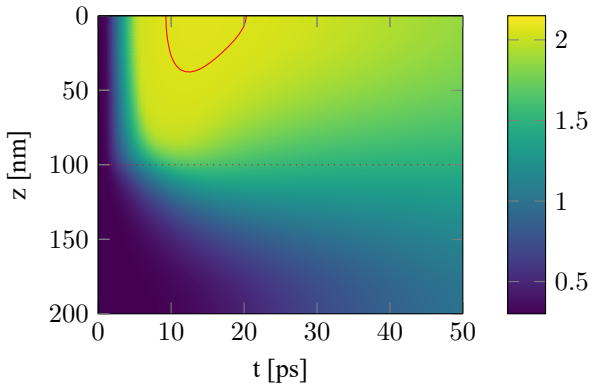

(c) Lattice temperature T_l for a peak fluence of $F = 0.43\,\mathrm{J/cm^2}$. The maximum reached temperature is $T_{l,\max} = 2101.6\,\mathrm{K}$.

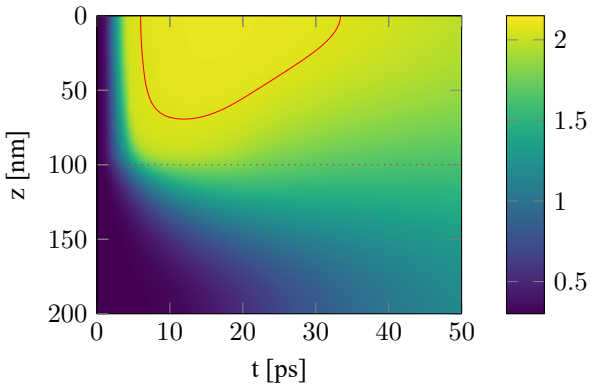

(d) Lattice temperature T_l for a peak fluence of $F = 0.86\,\mathrm{J/cm^2}$. The maximum reached temperature is $T_{l,\max} = 2104.9\,\mathrm{K}$.

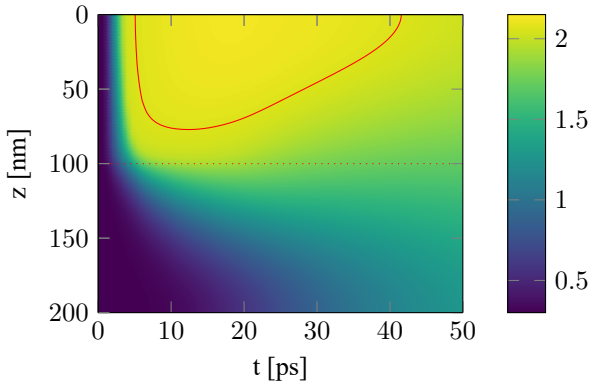

(e) Lattice temperature T_l for a peak fluence of $F = 1.29\,\mathrm{J/cm^2}$. The maximum reached temperature is $T_{l,\max} = 2132.5\,\mathrm{K}$.

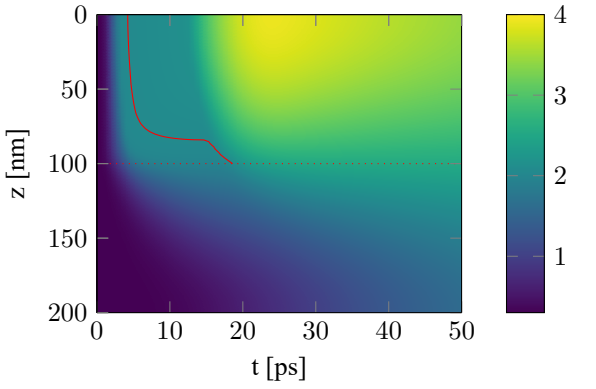

(f) Lattice temperature T_l for a peak fluence of $F = 2.15\,\mathrm{J/cm^2}$. The maximum reached temperature is $T_{l,\max} = 3926.4\,\mathrm{K}$. Please note the different colorbar.

Fig. 7 Computation of the lattice temperature distribution $T_l(z,t)$ in $10^3\,\mathrm{K}$ within a 100 nm ITO film for peak fluences of $F = 0.22\,\mathrm{J/cm^2}$ to $2.15\,\mathrm{J/cm^2}$. The red contour line indicates the region where $T_l \geq T_{\mathrm{melt,ITO}}$. For figs. 7a to 7e the colorbars range from 300 K to 2150 K and for fig. 7f from 300 K to 4000 K, respectively

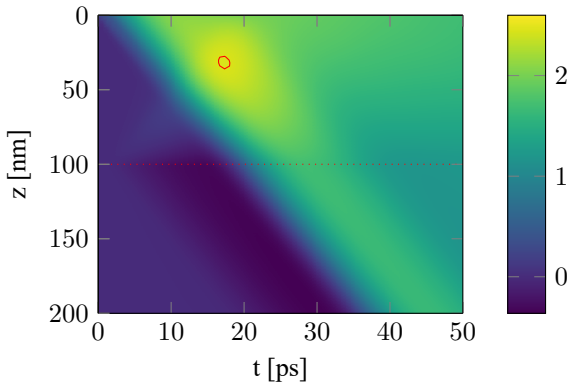

(a) Strain ϵ_{zz} for a peak fluence of $F = 0.22\,\mathrm{J/cm^2}$. The maximum reached strain is $\epsilon_{zz} = 2.458\%$.

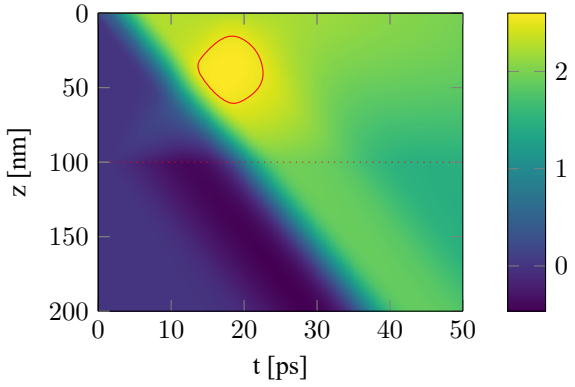

(b) Strain ϵ_{zz} for a peak fluence of $F = 0.32\,\mathrm{J/cm^2}$.The maximum reached strain is $\epsilon_{zz} = 2.463\%$.

Fig. 8 Computation of the strain distribution ϵ_{zz} in % within a 100 nm ITO film for peak fluences of $F = 0.22\,\mathrm{J/cm^2}$ and $F = 0.32\,\mathrm{J/cm^2}$.

region where the temperature exceeds the melting temperature $T_l \geq T_{\mathrm{melt,ITO}}$ is 79 nm while the measured depth is around 73 nm. Fluences larger than $F \geq 2.15\,\mathrm{J/cm^2}$ lead to melting of the whole 100 nmITO film which can also be seen experimentally (c.f. fig. 2).

It is worth to mention, that the elastic model is only valid if the mass density ρ is constant, no plastic deformations occur and/or the lattice temperatures do not exceed the melting temperature. The last requirements are not valid for peak fluences $F > 0.35\,\mathrm{J/cm^2}$ since $T_l \geq T_{\mathrm{melt,ITO}}$. For this reason, the computed strains for these fluences should be considered with care since they should be damped due to plastic deformations.

5. Conclusion

In this study, we extended a dual hyperbolic two temperature model for the electron and lattice temperatures with transient optical properties. The transient optical properties result from free electron dynamics to accurately describe the excitation of the electronic subsystem with ultrashort laser pulses. The excitation of free electrons is modeled using rate equations and results in shielding of the laser pulse intensity due to a rise in reflectivity to up to $R \approx 90\%$. Simultaneously, depending on the fluence, the optical penetration depth decreases from 2.2 µm to only a few 10 nm. To adequately describe the heat source for the two temperature model consideration of the transient optical properties and the latent heat was necessary.

We successfully identified the relevant ablation mechanisms of 100 nm ITO films for peak fluences up to $4.3\,\mathrm{J/cm^2}$: $F \leq 0.35\,\mathrm{J/cm^2}$ the ablation mechanism is mechanical. Here the ablation criterion is $\epsilon_{zz} \geq \epsilon_{yield}$. For higher peak fluences $F > 0.35\,\mathrm{J/cm^2}$ lattice temperatures exceed the melting temperature of ITO. Hence, the ablation criterion for higher peak fluences is $T_l \geq T_{\mathrm{melt,ITO}}$. However, the fluence reduces in radial direction according to the Gaussian fluence distribution. Therefore, the fluences in the marginal areas of the craters are smaller than the peak fluence $F < 0.35\,\mathrm{J/cm^2}$. Thus, the ablation mechanism is both thermal and mechanical. The computed mechanical strains and lattice temperatures agree with measured ablation craters.

The dynamical TTM model for thin ITO films leads to a better understanding of the underlying ablation mechanisms during the ablation process with ultrashort pulsed laser radiation. This enables predictive simulation of the ablation process. To get a more comprehensive numerical description of the ablation process and to check the applicability of effective optical properties, plasticity and the laser propagation within the layered sample could be considered. To numerically investigate the melting and the melt dynamics and ejection, hydrodynamic equations or molecular dynamic simulations should be solved.

Acknowledgement

Funded by the Deutsche Forschungsgemeinschaft (DFG, German Research Foundation) — 423531130. Additionally, the interesting, instructive and fruitful discussions with Markus Niessen and Christian Heinigk are greatly appreciated.

References

[1] D. S. Ginley and C. Bright: MRS Bull, 25, (2000) 15.

[2] K. Ellmer: Nat. Photonics, 6, (2012) 809.

[3] P. M. Harrison, N. Hay, and D. P. Hand: Appl. Surf. Sci., 256, (2010) 7276.

[4] J. C. C. Fan and J. B. Goodenough: J. Appl. Phys., 48, (1977) 3524.

[5] J. Du, X.-l. Chen, C.-c. Liu, J. Ni, G.-f. Hou, Y. Zhao, and X.-d. Zhang: Appl. Phys., 117, (2014) 815.

[6] A. Rämer, O. Osmani, and B. Rethfeld: J. Appl. Phys., 116, (2014) 053508.

[7] D. Kürschner, G. Hallum, S. Vogel, H. P. Huber, and W. Schulz: Int. J. Heat Mass Transf., 209, (2023) 124119.

[8] G. E. Jellison and F. A. Modine: Appl. Phys. Lett., 69, (1996) 371.

[9] M. Fox: “Optical properties of solids”, (Oxford Univ. Press, Oxford, 2008) p.154.

[10] K. Sokolowski-Tinten and D. von der Linde: Phys. Rev. B, 61, (2000) 2643.

[11] J. Noack and A. Vogel: IEEE J Quantum Electron, 35, (1999) 12.

[12] A. Vogel, J. Noack, G. Hüttman, and G. Paltauf: Appl. Phys. B, 81, (2005) 1015.

[13] L. W. van Beveren, E. Panchenko, N. Anachi, L. Hyde, D. Smith, T. James, A. Roberts, and J. McCallum: Proc. COMMAD 2014, (2014) 144.

[14] I. Hamberg, C. G. Granqvist, K. .-. Berggren, B. E. Sernelius, and L. Engström: Phys. Rev. B, 30, (1984) 3240.

[15] J. R. V. d. Aldana, C. Méndez, L. Roso, and P. Moreno: J. Phys. D, 38, (2005) 2764.

[16] M. Pitaro, E. K. Tekelenburg, S. Shao, and M. A. Loi: Adv. Mater., 34, (2022) 2105844.

[17] National Center for Biotechnology Information, PubChem: In1.69Sn0.15O2.85, (2023).

[18] S. Anisimov, B. Kapeliovich, and T. Perelman: Zh. Eksp. Teor. Fiz, 66, (1974) 375.

[19] J. Chen, J. Beraun, L. Grimes, and D. Tzou: Int J Solids Struct, 39, (2002) 3199.

[20] V. Kostrykin, M. Niessen, J. Jandeleit, W. Schulz, E.-W. Kreutz, and R. Poprawe: Proc. SPIE, Vol. 3343, (1998) 971.

[21] V. Gupta, A. Argon, D. Parks, and J. Cornie: J Mech Phys Solids, 40, (1992) 141.

[22] C. McDonnell, D.Milne, C. Prieto, H. Chan, D. Rostohar, and G. O'Connor: Appl. Surf. Sci., 359, (2015) 567.

[23] W. Marine, N. M. Bulgakova, L. Patrone, and I. Ozerov: J. Appl. Phys., 103, (2008) 094902.

[24] L. A. Falkovsky and E. G. Mishchenko: J. Exp. Theor. Phys., 88, (1999) 84.

[25] G. Mur: IEEE Trans Electromagn Compat, EMC-23, (1981) 377.

[26] T. Ashida, A. Miyamura, N. Oka, Y. Sato, T. Yagi, N. Taketoshi, T. Baba, and Y. Shigesato: J. Appl. Phys., 105, (2009) 073709.

[27] E. Medvedovski, N. Alvarez, O. Yankov, and M. K. Olsson: Ceram. Int, (2008) 10.

[28] C.-L. Tien and T.-W. Lin: Coatings, 11, (2021) 153.

[29] C. McDonnell, D. Milne, H. Chan, D. Rostohar, and G. O'Connor: Opt Lasers Eng, 81, (2016) 70.

[30] C. E. Protasov, R. S. Khmyrov, S. N. Grigoriev, and A. V. Gusarov: Int. J. Heat Mass Transf., 104, (2017) 665.

[31] H. J. Melosh: Meteorit Planet Sci, 42, (2007) 2079.

[32] M. Fukuhara and A. Sampei: J. Mater. Sci. Letters, 18, (1999) 751.

[33] M. Fukuhara, A. Sanpei, and K. Shibuki: J. Mater. Sci., 32, (1997) 1207.

[34] G. M. Graham and H. E. Hagy: Am J Phys, (1972) 13.

[35] D. W. Lee and W. D. Kingery: J. Am. Ceram. Soc., 43, (1960) 594.

[36] A. F. Bower: "Applied Mechanics of Solids", (CRC Press, Boca Raton, 2009) p.74.

[37] G. E. Hallum, D. Kürschner, D. Redka, D. Niethammer, W. Schulz, and H. P. Huber: Opt. Express, 29, (2021) 30062.

[38] M. Domke, S. Rapp, M. Schmidt, and H. P. Huber: Opt. Express, 20, (2012) 10330.

[39] D. Redka, C. Gadelmeier, J. Winter, M. Spellauge, C. Eulenkamp, P. Calta, U. Glatzel, J. Minár, and H. P. Huber: Appl. Surf. Sci., 544, (2021) 148839.

[40] D. R. Cairns, D. C. Paine, and G. P. Crawford: MRS OPL, 666, (2001) F3.24.

[41] L. E. Kinsler, A. R. Frey, A. B. Coppens, and J. V. Sanders: "Fundamentals of Acoustics", (John Wiley & Sons, Hoboken, 2000) p.150.

(Received: June 13, 2023, Accepted: November 19, 2023